ADVANCING EARTH AND SPACE SCIENCE

Geophysical Research Letters

RESEARCH LETTER
10.1029/2023GL102922

Chorus Wave Properties From Van Allen Probes: Quantifying the Impact of the Sheath Corrected Electric Field

D. P. Hartley[1], I. W. Christopher[1], C. A. Kletzing[1], W. S. Kurth[1], O. Santolik[2,3], I. Kolmasova[2,3], M. R. Argall[4], and N. Ahmadi[5]

[1]Department of Physics and Astronomy, University of Iowa, Iowa City, IA, USA, [2]Department of Space Physics, Institute of Atmospheric Physics, Prague, Czech Republic, [3]Faculty of Mathematics and Physics, Charles University, Prague, Czech Republic, [4]Space Science Center, Institute for the Study of Earth, Oceans, and Space, University of New Hampshire, Durham, NH, USA, [5]Laboratory for Atmospheric and Space Physics, University of Colorado Boulder, Boulder, CO, USA

Key Points:

- Sheath-correction results in increase of electric field chorus wave power by a factor of 2–9, and increase in Poynting flux by factor of ~2
- Sheath correction causes the Poynting vector to switch hemispheres, from parallel to anti-parallel propagation, in only ~2% of cases
- Theoretically predicted relationship between wave vector and Poynting vector is well-reproduced with sheath-corrected data

Correspondence to:

D. P. Hartley,
david-hartley@uiowa.edu

Citation:

Hartley, D. P., Christopher, I. W., Kletzing, C. A., Kurth, W. S., Santolik, O., Kolmasova, I., et al. (2023). Chorus wave properties from Van Allen Probes: Quantifying the impact of the sheath corrected electric field. *Geophysical Research Letters*, *50*, e2023GL102922. https://doi.org/10.1029/2023GL102922

Received 30 JAN 2023
Accepted 16 MAR 2023

Abstract

A sheath impedance model has recently been developed to describe how the variable coupling impedance between the Van Allen Probes instrumentation and the ambient plasma affects both the amplitude and phase of electric field wave measurements. Here, the impact of this sheath correction on measured chorus wave properties, including electric field wave power and the Poynting vector, is directly quantified. It is found that the sheath-corrected electric field wave power is typically between two and nine times larger than the uncorrected measurement, depending on wave frequency. The sheath correction typically increases the Poynting flux by a factor of ~2, and causes the polar angle of the Poynting vector to switch hemisphere from parallel to anti-parallel propagation in ~2% of cases. The uncorrected data exhibit significant deviations from the theoretically predicted relationship between the wave vector and the Poynting vector whereas this relationship is well-reproduced with the sheath-corrected observations.

Plain Language Summary

The wave electric field on Van Allen Probes has recently been corrected for sheath impedance effects, which can affect both the amplitude and phase of the measurements. Here, for the first time, we directly quantify the impact of this correction factor on chorus wave measurements of electric field wave power. We also investigate the impact on the Poynting vector direction and magnitude, which is itself determined from electric field observations and magnetic field measurements. It is found that after applying the sheath correction to chorus wave observations, the electric field wave power typically increases by a factor between two and nine, whereas the Poynting flux typically increases by a factor of ~2. The relationship between the wave vector and the Poynting vector is compared to that expected from cold plasma theory, for both the corrected and uncorrected observations. Significant differences between observations and theory are apparent when using the uncorrected measurements, however the sheath-corrected observations agree well with the theoretical predictions.

1. Introduction

Whistler-mode chorus waves play an important role in driving radiation belt dynamics (Thorne et al., 2010), including rapid acceleration of electrons (Allison et al., 2021; Thorne et al., 2013) and particle loss to the atmosphere during microbursts (Breneman et al., 2017; Douma et al., 2018; Lorentzen et al., 2001; Mozer et al., 2018; Shumko et al., 2018, 2021) and diffuse auroral precipitation (Newell, 2010; Ni et al., 2011; Nishimura et al., 2010; Thorne et al., 2010). Chorus is typically observed between ~100 Hz and several kHz (Gurnett & O'Brien, 1964), scaling between 0.05 and 0.90f_{ce}, where f_{ce} is the equatorial electron cyclotron frequency. A minimum in power is often observable at 0.50f_{ce} (Koons & Roeder, 1990; Li et al., 2019; Tsurutani & Smith, 1974).

The Van Allen Probes (Mauk et al., 2012) measure the electric field using spherical double probe sensors. These sensors, part of the Electric Field and Waves (EFW) instrument (Wygant et al., 2013), are electrically coupled to the magnetospheric plasma through a plasma sheath which forms around the sensors. This instrument-plasma coupling can attenuate the measured output voltage and thus leads to a frequency-dependent response function which varies with the local plasma environment, affecting both the amplitude and phase of the observations. Due to differences between the electric field instrument for each axis, the instrument-plasma interface is different between the spin-plane and spin-axis measurements. Additionally, due to the shorter booms used along the spin-axis, this measurement direction is more susceptible to the electrical shortening that can occur

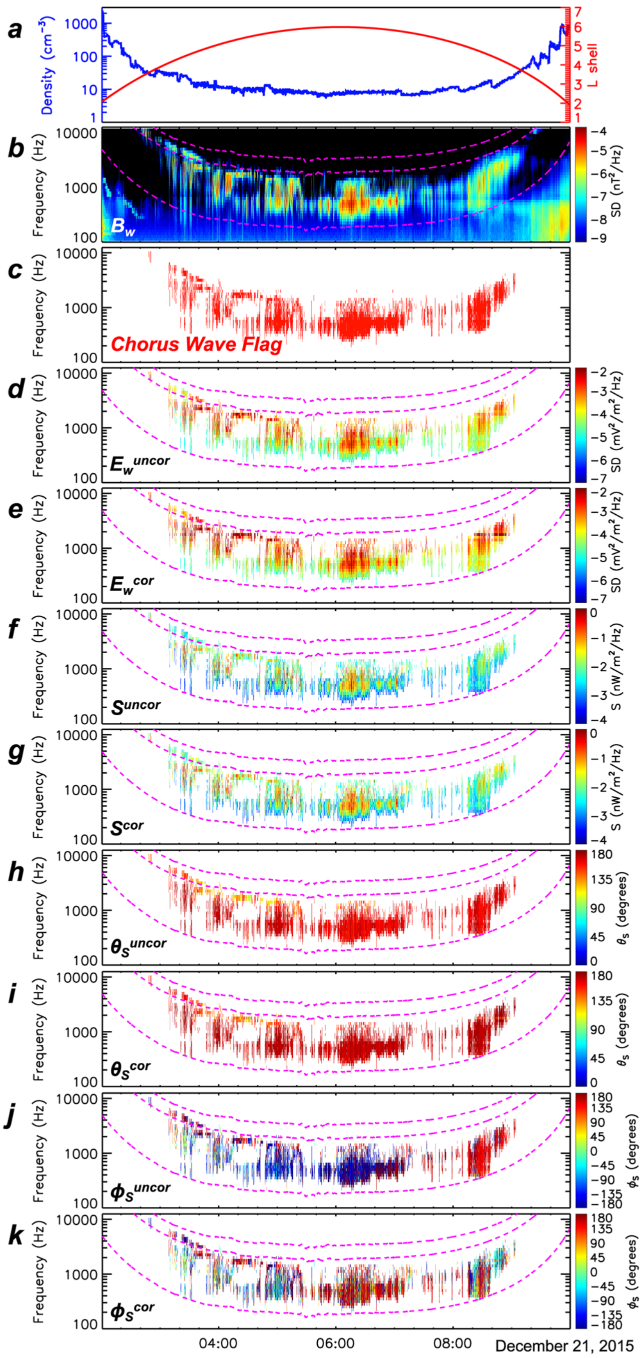

Figure 1. RBSP-A measurements of, (a) plasma density and L, (b) magnetic field power spectral density, B_w, (c) chorus wave flag, (d) uncorrected electric field power spectral density, E_w^{uncor}, (e) sheath-corrected electric field power spectral density, E_w^{cor}, (f) uncorrected Poynting flux, S^{uncor}, (g) sheath-corrected Poynting flux, S^{cor}, (h) polar angle of uncorrected Poynting vector, θ_S^{uncor}, (i) polar angle of sheath-corrected Poynting vector, θ_S^{cor}, (j) azimuthal angle of uncorrected Poynting vector, ϕ_S^{uncor}, and (k) azimuthal angle of sheath-corrected Poynting vector, ϕ_S^{cor}. Dashed pink lines are 0.05, 0.50, and $0.90f_{ce}$.

when the Debye length becomes comparable to the antenna length (Califf & Cully, 2016; Cully et al., 2007; Khotyaintsev et al., 2014; Lejosne & Mozer, 2019; Pedersen et al., 1998; Mozer et al., 1974). A model has been developed to correct for these effects (Hartley, Christopher, et al., 2022). Since signals from EFW are passed to the Electric and Magnetic Field Instrument Suite and Integrated Science (EMFISIS) Waves instrument for FFT processing (Kletzing et al., 2013), a full sheath-corrected EMFISIS data set was produced for final data archive.

Sheath effects are most prevalent at low density (Hartley, Christopher, et al., 2022; Hartley et al., 2015, 2016, 2017) where chorus is commonly observed, and primarily impact spin-axis measurements. To date, there has been no quantification of how chorus wave properties, including electric field wave power and Poynting vector observations, are impacted by the sheath correction. Here, this is achieved by directly comparing the uncorrected measurements with the sheath-corrected data.

Evaluating this impact is important as numerous studies have investigated the electric field chorus wave power (Li et al., 2016; Tyler et al., 2019), in part, because the high-amplitude parallel electric field associated with oblique chorus (Cattell et al., 2008) can drive nonlinear electron acceleration through Landau resonance (Agapitov et al., 2014; Artemyev et al., 2012, 2013). Additionally, the Poynting vector (which requires electric field observations to compute) describes the propagation of wave energy, and is a crucial quantity for determining the location, size, and dynamics of the chorus source region (LeDocq et al., 1998; Nagano et al., 1996; Parrot et al., 2003; Santolik et al., 2004, 2005; Taubenschuss et al., 2016; Teng et al., 2018), as well as for describing chorus propagation (Cattell et al., 2015; Chen et al., 2021; Colpitts et al., 2020; Demekhov et al., 2017; Hartley, Chen, et al., 2022; Santolik et al., 2006, 2009).

2. Chorus Wave Identification

As in previous studies (Bingham et al., 2018; Hartley et al., 2015, 2016, 2019; Li et al., 2014; Wang et al., 2019), waves are identified as chorus if they, (a) occur between $0.05f_{ce}$ and $0.90f_{ce}$, (b) occur when the plasma density (Kurth et al., 2015) is less than $10 \times (6.6/L)^4$ or 30 cm^{-3}, whichever is smaller, (c) have planarity (Santolík et al., 2003) exceeding 0.6, and ellipticity (Santolík et al., 2002) and 2D degree of coherence in the polarization plane (Santolík & Gurnett, 2002) exceeding 0.5, and (d) have magnetic field wave power larger than the greater of 10^{-9} nT^2/Hz or 5× the instrument background levels.

These thresholds ensure right-handed waves which are approximately circularly polarized and meet the plane wave approximation. Note that these selection criteria are based on magnetic field observations only and are therefore unaffected by sheath effects, meaning that the same events are selected for both the uncorrected and sheath-corrected data. Note also that this selection procedure is not affected by the time-frequency structure on timescales below a few seconds, meaning the selected data contains not only chorus with discrete elements, but also "hiss-like" chorus (Li et al., 2012) and any hiss or exo-hiss (Zhu et al., 2015) that may be coherent (Summers et al., 2014; Tsurutani et al., 2015), all of which may exist without clear time-frequency signatures. For simplicity, waves that meet the above described selection procedure are referred to as chorus waves throughout this paper.

Figure 1 provides an example of this wave identification procedure showing (a) plasma density (blue) and L shell (red), (b) power spectral density of the magnetic field, B_w, and (c) the chorus wave flag. For waves flagged as

10.1029/2023GL102922

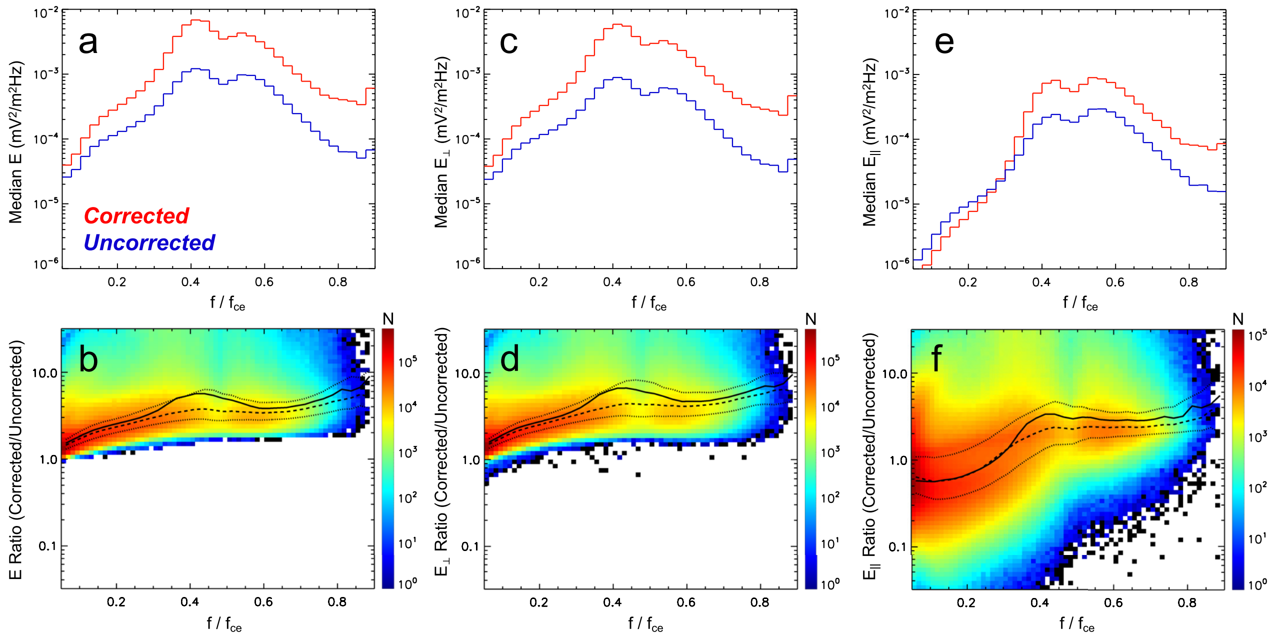

Figure 2. Median uncorrected (blue) and sheath-corrected (red) electric field power spectra for (a) total wave power, (c) wave power perpendicular to $\mathbf{B_0}$, and (e) wave power parallel to $\mathbf{B_0}$. Ratio between corrected and uncorrected median spectra, $\mathbf{M}(E_w^{cor})/\mathbf{M}(E_w^{uncor})$, where $\mathbf{M}$ denotes the median of the value in parenthesis, is shown by the solid line for (b) total wave power, (d) perpendicular wave power, and (f) parallel wave power. Also shown is the distribution formed by taking the ratio between uncorrected and sheath-corrected data for each measurement (color), with the median ($\mathbf{M}(E_w^{cor}/E_w^{uncor})$, dashed line) and the 25th and 75th percentiles (dotted lines) also provided.

chorus, the power spectral density (SD) of the electric field is shown for (d) uncorrected measurements, E_w^{uncor}, and (e) sheath-corrected measurements E_w^{cor}. The Poynting flux is shown for (f) uncorrected observations, S^{uncor}, and (g) sheath-corrected observations, S^{cor}. The polar and azimuthal angles of the Poynting vector are shown in (h) and (j) for the uncorrected data, θ_S^{uncor} and ϕ_S^{uncor}, and (i) and (k) for the sheath-corrected data, θ_S^{cor} and ϕ_S^{cor}. All sheath-corrected values are based on the correction provided by Hartley, Christopher, et al. (2022).

It is immediately evident that differences exist between the uncorrected and sheath-corrected observations, with both $E_w^{cor} > E_w^{uncor}$ and $S^{cor} > S^{uncor}$, as well as differences between ϕ_S^{cor} and ϕ_S^{uncor}. This chorus identification procedure is applied to measurements from both Van Allen Probes spacecraft over the full mission duration, resulting in a database containing 14,815,703 individual frequency-time observations across 3,635,626 unique time intervals. This allows us to conduct direct comparisons between the uncorrected and sheath-corrected observations in a statistical analysis and to quantify the differences.

3. The Impact on Electric Field Observations

Figure 2a shows the median power spectral density of E_w^{uncor} (blue) and E_w^{cor} (red) as a function of normalized wave frequency, f/f_{ce}. These median power spectral density values are expressed as $\mathbf{M}(E_w^{uncor})$ and $\mathbf{M}(E_w^{cor})$ hereafter, with $\mathbf{M}$ denoting the median of the value in parenthesis. Both the ratio of these median values ($\mathbf{M}(E_w^{cor})/\mathbf{M}(E_w^{uncor})$) and the median of the ratios ($\mathbf{M}(E_w^{cor}/E_w^{uncor})$) are calculated. Figure 2b (solid line) shows the ratio between these median spectra, $\mathbf{M}(E_w^{cor})/\mathbf{M}(E_w^{uncor})$. For waves near $0.05f_{ce}$, $\mathbf{M}(E_w^{cor})$ is a factor of ~2 larger than $\mathbf{M}(E_w^{uncor})$. This factor increases with increasing wave frequency up to a local maximum of ~6 near $0.40f_{ce}$, decreases down to ~4 near $0.60f_{ce}$, before increasing again to a factor of ~9 by $0.90f_{ce}$. For context, Figure 2b also shows the distribution formed by taking the ratio between E_w^{uncor} and E_w^{cor} for each individual observation (color), with the median ratio, $\mathbf{M}(E_w^{cor}/E_w^{uncor})$ (dashed line) and corresponding 25th and 75th percentiles (dotted lines) also shown. The median of the ratios, $\mathbf{M}(E_w^{cor}/E_w^{uncor})$, exhibits a similar behavior to the ratio of the medians, $\mathbf{M}(E_w^{cor})/\mathbf{M}(E_w^{uncor})$, albeit with some deviations occurring for 0.35–$0.55f_{ce}$, likely attributable to skew in the underlying distributions. The number of data points (colors) indicate a sharp lower cutoff at a ratio ~1–2 and a long tail up to high ratio values (>10). The 25th and 75th percentiles (dotted lines) indicate that, despite this long tail, the majority of data are relatively tightly bound to the median.

10.1029/2023GL102922

Electric field observations are then sorted into wave power that is perpendicular to, $E_{w\perp}$ (Figures 2c and 2d), and parallel to, $E_{w\parallel}$ (Figures 2e and 2f), the background magnetic field, $\mathbf{B_0}$. The median spectra of $E_{w\perp}^{uncor}$ and $E_{w\perp}^{cor}$ look largely similar to those for E_w^{uncor} and E_w^{cor}. The ratio of the median spectra, $\mathbf{M}\left(E_{w\perp}^{cor}\right)/\mathbf{M}\left(E_{w\perp}^{uncor}\right)$ (solid line in Figure 2d), is ∼2 for the lowest frequencies, increases to ∼7 at $0.40f_{ce}$, decreases to ∼5 at $0.60f_{ce}$, and increases to almost 10 for the highest frequencies. However, the median spectra of $E_{w\parallel}$ show some differences, with $\mathbf{M}\left(E_{w\parallel}^{cor}\right) < \mathbf{M}\left(E_{w\parallel}^{uncor}\right)$ at frequencies below $\sim 0.25f_{ce}$. For frequencies greater than $\sim 0.25f_{ce}$, $\mathbf{M}\left(E_{w\parallel}^{cor}\right) > \mathbf{M}\left(E_{w\parallel}^{uncor}\right)$. This is quantified by the ratio of the median spectra, $\mathbf{M}\left(E_{w\parallel}^{cor}\right)/\mathbf{M}\left(E_{w\parallel}^{uncor}\right)$ (solid line in Figure 2f), which is less than unity for frequencies below $0.25f_{ce}$ with a minimum near 0.6 at the lowest frequencies. It then rises to ∼3–4 near $0.40f_{ce}$, where it remains for frequencies up to $0.80f_{ce}$, before increasing to values between ∼4 and 6 for the highest frequencies. For both $E_{w\perp}$ and $E_{w\parallel}$, the median of the ratio values (dashed lines) exhibit a very similar behavior to the ratios of the respective medians (solid line).

This analysis reveals that the sheath correction generally has a larger impact on $E_{w\perp}$ than $E_{w\parallel}$. This is attributable to the spacecraft orientation, which results in the spin axis antenna, which has a larger correction factor, more frequently measuring $E_{w\perp}$ than $E_{w\parallel}$. It should be noted that there are occurrences where the ratios can deviate substantially from the median values. However, the direct comparison between the sheath-corrected and uncorrected values presented here is important given that $E_{w\parallel}$ and $E_{w\perp}$ can accelerate electrons through Landau and cyclotron resonances (e.g., Agapitov et al., 2015, 2016; Artemyev et al., 2016; Chen et al., 2019; Min et al., 2014; Omura et al., 2019).

4. The Impact on Poynting Vector Direction and Magnitude

In a similar manner to the electric field analysis presented above, the median Poynting flux spectra is determined from the uncorrected, S^{uncor}, and sheath-corrected, S^{cor}, observations, denoted as $\mathbf{M}(S^{uncor})$ and $\mathbf{M}(S^{cor})$, respectively. These spectra are shown in Figure 3a with $\mathbf{M}(S^{uncor})$ in blue and $\mathbf{M}(S^{cor})$ in red, with the ratio between them, $\mathbf{M}(S^{cor})/\mathbf{M}(S^{uncor})$, shown in Figure 3b (solid line). In contrast to the electric field observations, $\mathbf{M}(S^{cor})/\mathbf{M}(S^{uncor})$ is relatively constant for all frequencies, with $\mathbf{M}(S^{cor})$ a factor of ∼2 greater than $\mathbf{M}(S^{uncor})$, with actual values varying between 1.30 and 2.55. The ratio of the median values, $\mathbf{M}(S^{cor})/\mathbf{M}(S^{uncor})$ (solid line), is equivalent to the median of the ratios, $\mathbf{M}(S^{cor}/S^{uncor})$ (dashed line), with both lines almost completely overlapping. The 25th and 75th percentiles (dotted lines) remain within ∼15% of the median value. The Poynting flux ratio distribution (colors) exhibits a larger spread toward higher ratio values than it does toward lower ratio values.

The sheath correction also affects the direction of the Poynting vector, which is defined by two angles: the polar angle, θ_S, (angle between $\mathbf{S}$ and $\mathbf{B_0}$), and the azimuthal angle, ϕ_S (angle around $\mathbf{B_0}$ with respect to the anti-Earthward direction). Here, we first investigate how the sheath correction impacts θ_S. Figure 3c shows the distribution of θ_S^{uncor} as a function of f/f_{ce}, with colors indicating the number of data. Black lines show the median θ_S value for both $\theta_S < 90°$ and $\theta_S > 90°$. Figure 3c demonstrates that S^{uncor} is typically oriented either quasi-parallel ($\theta_S < 30°$) or quasi-antiparallel ($\theta_S > 150°$). The median value is typically ∼12°–30° from field-aligned (or anti-field-aligned). Figure 3d is in the same format as Figure 3c but shows θ_S^{cor}. The median θ_S^{cor} value varies from ∼5°–20°, demonstrating that the sheath correction typically causes the Poynting vector to become more closely aligned with $\mathbf{B_0}$.

Figure 3e shows the absolute value of the difference between θ_S^{uncor} and θ_S^{cor} as a function of f/f_{ce}. This difference is often small, but can be substantial in some instances. $|\theta_S^{uncor} - \theta_S^{cor}|$ is less than 10° for 64% of observations, between 10° and 20° for 27% of observations, between 20° and 30° for 5% of observations, and greater than 30° for 4% of observations.

Singular Value Decomposition (SVD) is used to determine the wave vector direction (Santolík et al., 2003), resulting in two possible solutions, one with a component of the wave vector parallel to the background magnetic field, and one with a component antiparallel to the background field. θ_S is used to remove this ambiguity and correctly define the wave vector direction, since the Poynting vector must exist in the same hemisphere as the wave vector. As such, the crucial quantity is whether $\theta_S < 90°$ or $\theta_S > 90°$.

It is evident in Figure 3e that $|\theta_S^{uncor} - \theta_S^{cor}| > 90°$ in some instances. This means that applying the sheath correction must result in the Poynting vector switching hemisphere, although we note that for oblique θ_S values a difference less than 90° may also result in the Poynting vector changing hemisphere. As such, we directly compute the

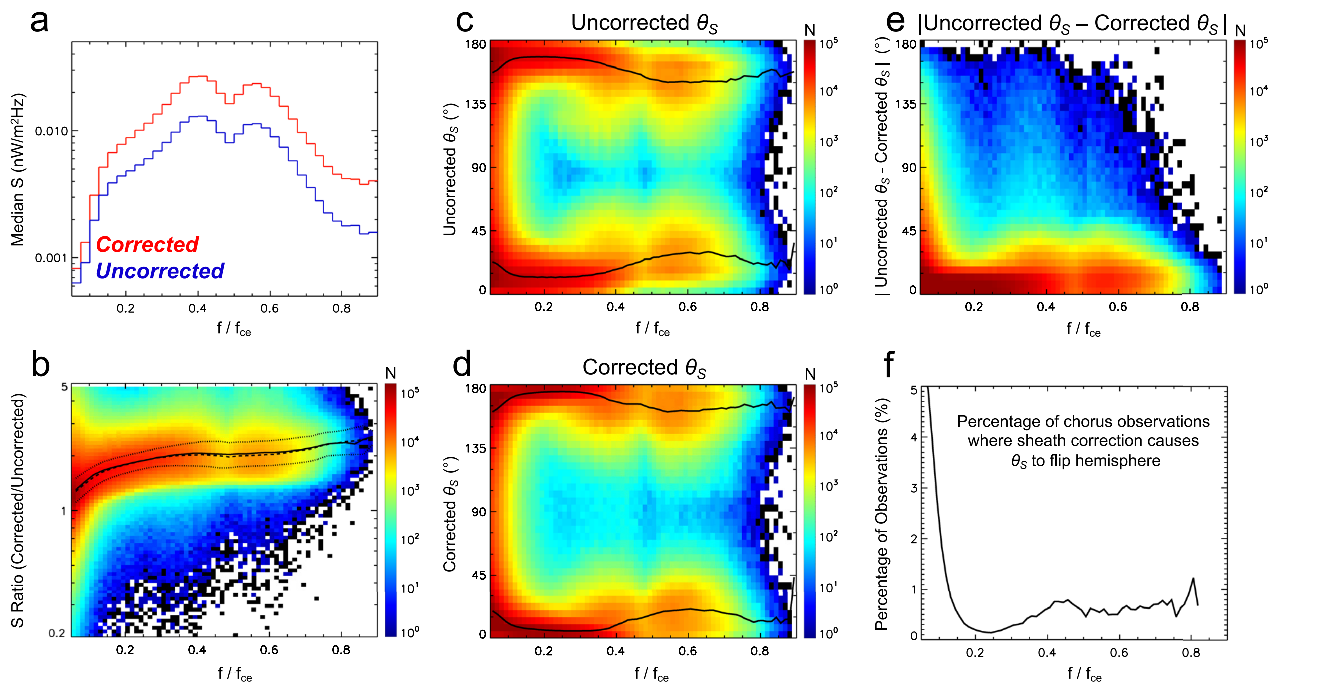

Figure 3. (a) Median spectral estimates of Poynting flux from uncorrected (blue) and sheath-corrected (red) data. (b) Ratio of median uncorrected and median sheath-corrected Poynting flux (solid line) from panel (a). Also shown (color) is the distribution formed by taking the ratio between the uncorrected and sheath-corrected Poynting flux measurement for each individual observation, with the median (dashed line) and the 25th and 75th percentiles (dotted lines) also provided. Polar angle of the Poynting vector, θ_S for (c) uncorrected and (d) sheath-corrected data, with median values overplotted in black. (e) Absolute value of the sheath-corrected θ_S subtracted from the uncorrected θ_S. (f) The percentage of chorus wave observations where θ_S changes hemisphere when the sheath correction is applied.

percentage of observations where the sheath correction results in the Poynting vector switching hemisphere, as shown in Figure 3f as a function of f/f_{ce}. At low frequency, this can be as high as 5.4%, but for frequencies above $0.125f/f_{ce}$ the percentage drops below 1%, and is typically only a few tenths of a percent. Overall, for all frequencies, it is found that S^{cor} is in the same hemisphere as S^{uncor} (parallel or anti-parallel to the background magnetic field) in ~98% of cases. That is, the sheath correction causes the Poynting vector to flip hemispheres in only ~2% of cases, with most of these cases at low frequency. As such, previous studies which used θ_S to determine the location, scale size, and dynamics of the chorus source region and chorus wave propagation characteristics are likely to achieve very similar results if repeated using the sheath-corrected data.

5. Comparison Between Wave Vector and Poynting Vector

For whistler-mode waves in a cold plasma, a theoretical relationship exists between the relative directions of the wave vector and the Poynting vector (Taubenschuss et al., 2016). Figure 4a shows the refractive index surface in a cold plasma in the field-aligned coordinate system where the $f = 1.5$ kHz, $f_{ce} = 10$ kHz, and $f_{pe} = 20$ kHz. The resonance cone and the Gendrin angle, θ_G (Gendrin, 1961), are shown by dashed and dotted lines, respectively. For each wave vector direction, the Poynting vector is normal to the refractive index surface. Here, we consider two wave vector directions defined by $\mathbf{k_1}$ (red) and $\mathbf{k_2}$ (blue). For $\mathbf{k_1}$, $\theta_{k1} < \theta_G$, which results in both $\mathbf{k_1}$, and the Poynting vector, $\mathbf{S_1}$, oriented in the positive $n_\perp$ direction. For $\mathbf{k_2}$, $\theta_{k2} > \theta_G$, resulting in $\mathbf{k_2}$ being oriented in the positive $n_\perp$ direction, but the Poynting vector, $\mathbf{S_2}$, being oriented in the negative $n_\perp$ direction. As such, the absolute value of azimuthal wave vector angle subtracted from the azimuthal angle of the Poynting vector, $|\phi_S - \phi_k|$, is equal to 0° in the case of $\mathbf{k_1}$ and $\mathbf{S_1}$, but equal to 180° in the case of $\mathbf{k_2}$ and $\mathbf{S_2}$. This theoretical relationship should remain true for all wave vector directions. That is, $|\phi_S - \phi_k| = 0°$ for $\theta_k < \theta_G$, and $|\phi_S - \phi_k| = 180°$ for $\theta_k > \theta_G$. Here, we explore the validity of this relationship using both the uncorrected and sheath-corrected observations.

As previously mentioned, θ_S is used to place the wave vector in the appropriate hemisphere and correctly define the wave vector direction. Once this adjustment to ϕ_k has been performed, we consider the probability distribution of ϕ_k, which is shown in Figure 4b for cases where $\theta_k < \theta_G$ (red) and $\theta_k > \theta_G$ (blue). Here, probability is defined as

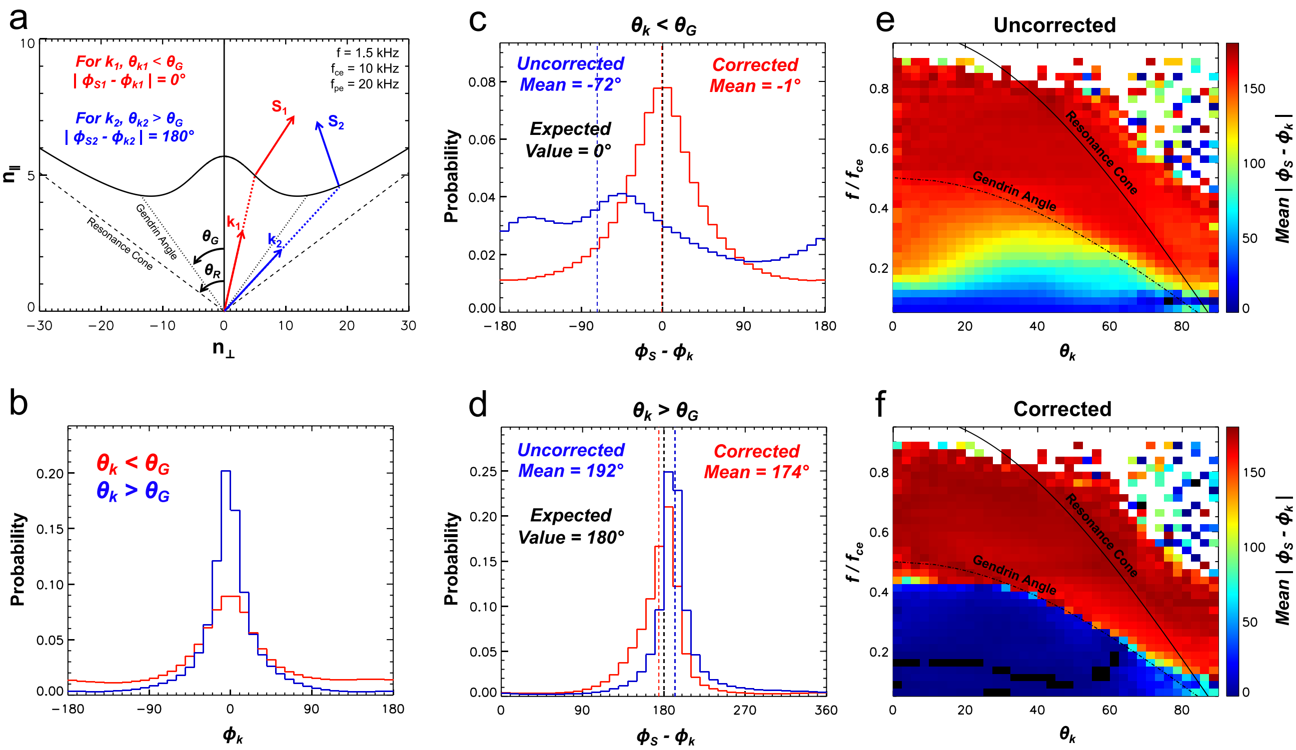

Figure 4. (a) Relationship between the wave vector, **k**, and Poynting vector, **S**, predicted from cold plasma theory. (b) Histograms showing probability distributions of the azimuthal direction of **k** for (red) $\theta_k < \theta_G$ and (blue) $\theta_k > \theta_G$. The difference between ϕ_S and ϕ_k for the (blue) uncorrected and (red) sheath-corrected data for (c) $\theta_k < \theta_G$ and (d) $\theta_k > \theta_G$. The mean of the absolute difference between ϕ_S and ϕ_k for (e) uncorrected and (f) sheath-corrected electric field observations.

the number of occurrences in each bin divided by the total number of occurrences. For both $\theta_k < \theta_G$ and $\theta_k > \theta_G$, the distribution is peaked near $\phi_k = 0°$ (anti-Earthward). For $\theta_k < \theta_G$ the wave vector is more field-aligned, meaning there is intrinsically more scatter in the distribution of ϕ_k, as small variations in the direction of **k** can result in large changes in ϕ_k. For $\theta_k > \theta_G$ the distribution is very strongly peaked in the anti-Earthward direction. In these cases, ϕ_k is well-defined due to the more oblique propagation. This feature of ϕ_k, being peaked in the anti-Earthward direction, has been previously reported (Taubenschuss et al., 2016; Hartley, Chen, et al., 2022; Hartley et al., 2019) and is a propagation effect that is well-modeled by ray tracing (e.g., Chum and Santolik (2005); Santolik et al. (2006)).

Given the strongly peaked distribution of ϕ_k in the anti-Earthward direction, it is expected that ϕ_S will present a distribution predominantly peaked anti-Earthward direction if $\theta_k < \theta_G$, and Earthward direction if $\theta_k > \theta_G$. Here, we compute the difference between the azimuthal wave vector angle and the azimuthal Poynting vector angle, $\phi_S - \phi_k$, for each chorus wave observation. These distributions are shown for both the uncorrected (blue) and sheath-corrected (red) data in Figure 4c for cases when $\theta_k < \theta_G$, and in Figure 4d for cases when $\theta_k > \theta_G$.

For $\theta_k < \theta_G$ (Figure 4c), the uncorrected observations (blue) show a bimodal structure in the distribution of $\phi_S - \phi_k$, with one peak near $-45°$ and another near $-145°$. Overall, the distribution is quite broad around the two peaks. Given that θ_S generally becomes more field-aligned in the sheath-corrected data (as demonstrated in Figure 2), one might expect the distribution of $\phi_S - \phi_k$ to become broader when using the sheath-corrected data set. In fact, the opposite is true, with the corrected observations (red) presenting a narrower, single-peaked distribution centered near 0°. This is much closer to the expected relation of $\phi_S - \phi_k = 0°$, as shown by the vertical dashed black line in Figure 4c. The mean of each distribution is also found by calculating $\arctan\left(\sum \sin(\phi_S - \phi_k), \sum \cos(\phi_S - \phi_k)\right)$, where the sum is over the total number of observations. These mean values are shown in Figure 4c for the uncorrected (blue) and sheath-corrected (red) distributions by vertical dashed lines. The mean of the uncorrected distribution is $-72°$, whereas the mean of the corrected distribution is $-1°$. This demonstrates that the uncorrected data display significant differences to the expected relationship between **k** and **S**, which are almost entirely rectified when using the sheath-corrected data.

For $\theta_k > \theta_G$, as shown in Figure 4d, both the uncorrected data (blue) and sheath-corrected observations (red) exhibit a single-peaked distribution in $\phi_S - \phi_k$. We center the plot around the expected peak of 180° (vertical dashed black line). It should be noted that the uncorrected and sheath-corrected distributions are offset from each other. To quantify this offset, the mean of each distribution is determined yielding 192° for the uncorrected data, and 174° for the sheath-corrected data, which are shown by vertical dashed blue and red lines, respectively. The mean of 192° in the uncorrected data means that, on average, there is a 12° offset from the expected value. This offset is only 6° for the corrected observations, again demonstrating that the sheath correction results in the relationship between **k** and **S** being more in line with what is expected from Figure 4a.

To explore the frequency dependence of the relationship between **k** and **S** we consider the mean difference between ϕ_S and ϕ_k as a function of wave normal angle, θ_k, and f/f_{ce}. We take the absolute value of this difference, so values of −45° and 45° are considered to be the same deviation from the expected value, and also limit $\phi_S - \phi_k$ values to be between 0° and 180°. These mean $|\phi_S - \phi_k|$ values are shown in Figures 4e and 4f for the uncorrected and sheath-corrected observations, respectively. The solid black line represents the resonance cone and the dot-dash line represents θ_G. For the uncorrected observations shown in Figure 4e, it is evident that for the majority of upper band chorus ($0.5 < f/f_{ce} < 0.9$), the difference between ϕ_S and ϕ_k is near, but not exactly, 180°. In general, values deviate further from 180° for frequencies near $0.5f_{ce}$. The corrected observations shown in Figure 4f present average values of $\phi_S - \phi_k$ very close to 180° for upper band chorus, with little variation with frequency. This relationship between **k** and **S** is expected, since all upper band chorus propagates with $\theta_k > \theta_G$ ($\theta_G = 0°$ above $0.5f_{ce}$).

For lower band chorus ($0.05 < f/f_{ce} < f0.50$), the uncorrected observations (Figure 4e) present a strong frequency dependence in the relationship between **k** and **S**. At frequencies near $0.05f_{ce}$, the azimuthal difference between **k** and **S** is near the expected value of 0°. But with increasing frequency, $|\phi_S - \phi_k|$ shifts away from 0° and by $0.20f_{ce}$ is close to 90°, even for θ_k values not near θ_G. For approximately field-aligned waves, between 0.25 and $0.50f_{ce}$ and $\theta_k < \theta_G$ the azimuthal difference between **k** and **S** is near 180°. In this region, there may be substantial scatter, as small fluctuations in the direction of **k** can result in large changes in ϕ_k. However, this relationship of $|\phi_S - \phi_k|$ being close to 180° remains apparent even for $\theta_k > 30°$ above $0.30f_{ce}$ and with $\theta_k < \theta_G$. This is in conflict with the expected relationship shown in Figure 4a.

For the sheath-corrected observations shown in Figure 4f, the relationship between **k** and **S** is much closer to that expected, with $|\phi_S - \phi_k|$ being near 0° for $\theta_k < \theta_G$ and being near 180° for $\theta_k > \theta_G$, with the transition being well-defined by the $\theta_k = \theta_G$ boundary. We do note some deviation from this expected relationship between 0.40 and $0.50f_{ce}$ for $\theta_k < 30°$. This may be attributable to multiple factors, including (a) the assumption of a dipole field when determining the equatorial f_{ce} value from local observations, (b) ϕ_k not being well-defined for small θ_k, (c) the discrete frequency bins in the EMFISIS survey data leading to blurring across the $f/f_{ce} = 0.50$ boundary, or (d) some other yet unknown effect.

Considering how sheath corrections can impact the direction of **S** in the context of previous works, we note that Taubenschuss et al. (2016) reported some deviations from the expected relationship between **k** and **S** which affected a few instances of lower band chorus and the majority of upper band chorus. Whilst their analysis was conducted using different instrumentation (THEMIS), sheath effects are universal to all electric field wave instruments and are therefore a possible explanation for the reported deviations.

Overall, comparison between Figures 4e and 4f demonstrates that the expected relationship between **k** and **S**, as shown in Figure 4a, is generally well-reproduced by the sheath-corrected data, whereas significant deviations from the expected relationship exist in the uncorrected observations.

6. Summary and Conclusions

In this study we have directly compared chorus wave parameters derived from both the uncorrected and sheath-corrected EMFISIS data from the Van Allen Probes, and statistically quantified the differences. The primary results may be summarized as:

1. The sheath-corrected electric field chorus wave power is between two and nine times larger than the uncorrected observations, depending on wave frequency.
2. In general, the sheath correction has a larger impact on the electric field wave power in the perpendicular direction, and less so in the parallel direction. This is due to the spacecraft orientation.

3. The sheath correction results in the chorus wave Poynting flux being around a factor of 2 larger than in the uncorrected observations.
4. The sheath correction causes the polar angle of the Poynting vector, θ_S to switch hemisphere in only ∼2% of chorus wave observations.
5. The theoretically predicted relationship between the wave vector, **k**, and the Poynting vector, **S**, is well-reproduced by the sheath-corrected data ($|\phi_k - \phi_S| = 0°$ for $\theta_k < \theta_G$ and $|\phi_k - \phi_S| = 180°$ for $\theta_k > \theta_G$), whereas the uncorrected observations show significant deviations from these expected values.

Overall, this study provides the first direct comparison between the sheath-corrected electric field observations and the uncorrected data product, quantifying the impact that the sheath correction has on chorus wave observations. These results help frame the context of previous studies based on uncorrected electric field wave observations by providing the community with statistically averaged values describing the impact of the sheath correction on chorus wave properties.

Data Availability Statement

All data used in this analysis is freely available and may be obtained from http://emfisis.physics.uiowa.edu/data/index or http://spdf.gsfc.nasa.gov/pub/data/rbsp/.

Acknowledgments
DPH, IWC, MRA and NA acknowledge that this material is based upon work supported by the National Aeronautics and Space Administration under Grant 80NSSC21K0519 issued through the Heliophysics Guest Investigators - Open 2020 Program. OS and IK acknowledge funding from the European Union's Horizon 2020 research and innovation programme under grant agreement No. 870452 and acknowledge support from MSMT Grant LUAUS23152.

References

Agapitov, O. V., Artemyev, A. V., Mourenas, D., Krasnoselskikh, V., Bonnell, J., Contel, O. L., et al. (2014). The quasi-electrostatic mode of chorus waves and electron nonlinear acceleration. *Journal of Geophysical Research: Space Physics*, *119*(3), 1606–1626. https://doi.org/10.1002/2013JA019223

Agapitov, O. V., Artemyev, A. V., Mourenas, D., Mozer, F. S., & Krasnoselskikh, V. (2015). Nonlinear local parallel acceleration of electrons through Landau trapping by oblique whistler mode waves in the outer radiation belt. *Geophysical Research Letters*, *42*(23), 10140–10149. https://doi.org/10.1002/2015GL066887

Agapitov, O. V., Mourenas, D., Artemyev, A. V., & Mozer, F. S. (2016). Exclusion principle for very oblique and parallel lower band chorus waves. *Geophysical Research Letters*, *43*(21), 11112–11120. https://doi.org/10.1002/2016GL071250

Allison, H. J., Shprits, Y. Y., Zhelavskaya, I. S., Wang, D., & Smirnov, A. G. (2021). Gyroresonant wave-particle interactions with chorus waves during extreme depletions of plasma density in the Van Allen radiation belts. *Science Advances*, *7*(5). https://doi.org/10.1126/sciadv.abc0380

Artemyev, A., Agapitov, O., Mourenas, D., Krasnoselskikh, V., Shastun, V., & Mozer, F. (2016). Oblique whistler-mode waves in the Earth's inner magnetosphere: Energy distribution, origins, and role in radiation belt dynamics. *Space Science Reviews*, *200*(1–4), 261–355. https://doi.org/10.1007/s11214-016-0252-5

Artemyev, A. V., Krasnoselskikh, V. V., Agapitov, O. V., Mourenas, D., & Rolland, G. (2012). Non-diffusive resonant acceleration of electrons in the radiation belts. *Physics of Plasmas*, *19*(12), 122901. https://doi.org/10.1063/1.4769726

Artemyev, A. V., Vasiliev, A. A., Mourenas, D., Agapitov, O. V., & Krasnoselskikh, V. V. (2013). Nonlinear electron acceleration by oblique whistler waves: Landau resonance vs. cyclotron resonance. *Physics of Plasmas*, *20*(12), 122901. https://doi.org/10.1063/1.4836595

Bingham, S. T., Mouikis, C. G., Kistler, L. M., Boyd, A. J., Paulson, K., Farrugia, C. J., et al. (2018). The outer radiation belt response to the storm time development of seed electrons and chorus wave activity during CME and CIR driven storms. *Journal of Geophysical Research: Space Physics*, *123*(12), 10139–10157. https://doi.org/10.1029/2018JA025963

Breneman, A. W., Crew, A., Sample, J., Klumpar, D., Johnson, A., Agapitov, O., et al. (2017). Observations directly linking relativistic electron microbursts to whistler mode chorus: Van Allen Probes and FIREBIRD II. *Geophysical Research Letters*, *44*(22), 11265–11272. https://doi.org/10.1002/2017GL075001

Califf, S., & Cully, C. M. (2016). Empirical estimates and theoretical predictions of the shorting factor for the THEMIS double-probe electric field instrument. *Journal of Geophysical Research: Space Physics*, *121*(7), 6223–6233. https://doi.org/10.1002/2016JA022589

Cattell, C., Wygant, J. R., Goetz, K., Kersten, K., Kellogg, P. J., von Rosenvinge, T., et al. (2008). Discovery of very large amplitude whistler-mode waves in Earth's radiation belts. *Geophysical Research Letters*, *35*(1), L01105. https://doi.org/10.1029/2007GL032009

Cattell, C. A., Breneman, A. W., Thaller, S. A., Wygant, J. R., Kletzing, C. A., & Kurth, W. S. (2015). Van Allen Probes observations of unusually low frequency whistler mode waves observed in association with moderate magnetic storms: Statistical study. *Geophysical Research Letters*, *42*(18), 7273–7281. https://doi.org/10.1002/2015GL065565

Chen, R., Gao, X., Lu, Q., Chen, L., Tsurutani, B. T., Li, W., et al. (2021). In situ observations of whistler-mode chorus waves guided by density ducts. *Journal of Geophysical Research: Space Physics*, *126*(4), e2020JA028814. https://doi.org/10.1029/2020JA028814

Chen, R., Gao, X., Lu, Q., & Wang, S. (2019). Unraveling the correlation between chorus wave and electron beam-like distribution in the Earth's magnetosphere. *Geophysical Research Letters*, *46*(21), 11671–11678. https://doi.org/10.1029/2019GL085108

Chum, J., & Santolík, O. (2005). Propagation of whistler-mode chorus to low altitudes: Divergent ray trajectories and ground accessibility. *Annals of Geophysics*, *23*(12), 3727–3738. https://doi.org/10.5194/angeo-23-3727-2005

Colpitts, C., Miyoshi, Y., Kasahara, Y., Delzanno, G. L., Wygant, J. R., Cattell, C. A., et al. (2020). First direct observations of propagation of discrete chorus elements from the equatorial source to higher latitudes, using the Van Allen Probes and Arase satellites. *Journal of Geophysical Research: Space Physics*, *125*(10), e2020JA028315. https://doi.org/10.1029/2020JA028315

Cully, C. M., Ergun, R. E., & Eriksson, A. I. (2007). Electrostatic structure around spacecraft in tenuous plasmas. *Journal of Geophysical Research*, *112*(A9), A09211. https://doi.org/10.1029/2007JA012269

Demekhov, A. G., Manninen, J., Santolík, O., & Titova, E. E. (2017). Conjugate ground-spacecraft observations of VLF chorus elements. *Geophysical Research Letters*, *44*(23), 11735–11744. https://doi.org/10.1002/2017GL076139

Douma, E., Rodger, C. J., Clilverd, M. A., Hendry, A. T., Engebretson, M. J., & Lessard, M. R. (2018). Comparison of relativistic microburst activity seen by SAMPEX with ground-based wave measurements at Halley, Antarctica. *Journal of Geophysical Research: Space Physics*, *123*(2), 1279–1294. https://doi.org/10.1002/2017JA024754

Gendrin, R. (1961). Le guidage des whistlers par le champ magnetique. *Planetary and Space Science*, *5*(4), 274–278. https://doi.org/10.1016/0032-0633(61)90096-4

Gurnett, D. A., & O'Brien, B. J. (1964). High latitude geophysical studies with satellite Injun 3: 5. Very low frequency electromagnetic radiation. *Journal of Geophysical Research*, *69*(1), 65–89. https://doi.org/10.1029/JZ069i001p00065

Hartley, D. P., Chen, L., Christopher, I. W., Kletzing, C. A., Santolik, O., Li, W., & Shi, R. (2022). The angular distribution of lower band chorus waves near plasmaspheric plumes. *Geophysical Research Letters*, *49*(9), e2022GL098710. https://doi.org/10.1029/2022GL098710

Hartley, D. P., Chen, Y., Kletzing, C. A., Denton, M. H., & Kurth, W. S. (2015). Applying the cold plasma dispersion relation to whistler mode chorus waves: EMFISIS wave measurements from the Van Allen probes. *Journal of Geophysical Research: Space Physics*, *120*(2), 1144–1152. https://doi.org/10.1002/2014JA020808

Hartley, D. P., Christopher, I. W., Kletzing, C. A., Kurth, W. S., Santolik, O., Kolmasova, I., et al. (2022). Quantifying the sheath impedance of the electric double probe instrument on the Van Allen Probes. *Journal of Geophysical Research: Space Physics*, *127*(5), e2022JA030369. https://doi.org/10.1029/2022JA030369

Hartley, D. P., Kletzing, C. A., Chen, L., Horne, R. B., & Santolík, O. (2019). Van Allen Probes observations of chorus wave vector orientations: Implications for the chorus-to-hiss mechanism. *Geophysical Research Letters*, *46*(5), 2337–2346. https://doi.org/10.1029/2019GL082111

Hartley, D. P., Kletzing, C. A., Kurth, W. S., Bounds, S. R., Averkamp, T. F., Hospodarsky, G. B., et al. (2016). Using the cold plasma dispersion relation and whistler mode waves to quantify the antenna sheath impedance of the Van Allen Probes EFW instrument. *Journal of Geophysical Research: Space Physics*, *121*(5), 4590–4606. https://doi.org/10.1002/2016JA022501

Hartley, D. P., Kletzing, C. A., Kurth, W. S., Hospodarsky, G. B., Bounds, S. R., Averkamp, T. F., et al. (2017). An improved sheath impedance model for the Van Allen Probes EFW instrument: Effects of the spin axis antenna. *Journal of Geophysical Research: Space Physics*, *122*(4), 4420–4429. https://doi.org/10.1002/2016JA023597

Khotyaintsev, Y. V., Lindqvist, P.-A., Cully, C. M., Eriksson, A. I., & Andre, M. (2014). In flight calibration of double-probe electric field measurements on Cluster. *Geoscientific Instrumentation, Methods and Data Systems*, *3*(2), 143–151. https://doi.org/10.5194/gi-3-143-2014

Kletzing, C. A., Kurth, W. S., Acuna, M., MacDowall, R. J., Torbert, R. B., Averkamp, T., et al. (2013). The electric and magnetic field instrument suite and integrated science (EMFISIS) on RBSP. *Space Science Reviews*, *179*(1–4), 127–181. https://doi.org/10.1007/s11214-013-9993-6

Koons, H. C., & Roeder, J. L. (1990). A survey of equatorial magnetospheric wave activity between 5 and 8 RE. *Planetary and Space Science*, *38*(10), 1335–1341. https://doi.org/10.1016/0032-0633(90)90136-E

Kurth, W. S., De Pascuale, S., Faden, J. B., Kletzing, C. A., Hospodarsky, G. B., Thaller, S., & Wygant, J. R. (2015). Electron densities inferred from plasma wave spectra obtained by the Waves instrument on Van Allen Probes. *Journal of Geophysical Research: Space Physics*, *120*(2), 904–914. https://doi.org/10.1002/2014JA020857

LeDocq, M. J., Gurnett, D. A., & Hospodarsky, G. B. (1998). Chorus source locations from VLF Poynting flux measurements with the Polar spacecraft. *Geophysical Research Letters*, *25*(21), 4063–4066. https://doi.org/10.1029/1998GL900071

Lejosne, S., & Mozer, F. S. (2019). Shorting factor in-flight calibration for the Van Allen Probes DC electric field measurements in the Earth's plasmasphere. *Earth and Space Science*, *6*(4), 646–654. https://doi.org/10.1029/2018EA000550

Li, J., Bortnik, J., An, X., Li, W., Angelopoulos, V., Thorne, R. M., et al. (2019). Origin of two-band chorus in the radiation belt of Earth. *Nature Communications*, *10*(1), 4672. https://doi.org/10.1038/s41467-019-12561-3

Li, W., Mourenas, D., Artemyev, A. V., Agapitov, O. V., Bortnik, J., Albert, J. M., et al. (2014). Evidence of stronger pitch angle scattering loss caused by oblique whistler-mode waves as compared with quasi-parallel waves. *Geophysical Research Letters*, *41*(17), 6063–6070. https://doi.org/10.1002/2014GL061260

Li, W., Santolik, O., Bortnik, J., Thorne, R. M., Kletzing, C. A., Kurth, W. S., & Hospodarsky, G. B. (2016). New chorus wave properties near the equator from Van Allen Probes wave observations. *Geophysical Research Letters*, *43*(10), 4725–4735. https://doi.org/10.1002/2016GL068780

Li, W., Thorne, R. M., Bortnik, J., Tao, X., & Angelopoulos, V. (2012). Characteristics of hiss-like and discrete whistler-mode emissions. *Geophysical Research Letters*, *39*(18), L18106. https://doi.org/10.1029/2012GL053206

Lorentzen, K. R., Blake, J. B., Inan, U. S., & Bortnik, J. (2001). Observations of relativistic electron microbursts in association with VLF chorus. *Journal of Geophysical Research*, *106*(A4), 6017–6027. https://doi.org/10.1029/2000JA003018

Mauk, B. H., Fox, N. J., Kanekal, S. G., Kessel, R. L., Sibeck, D. G., & Ukhorskiy, A. (2012). Science objectives and rationale for the radiation belt storm probes mission. *Space Science Reviews*, *179*(1–4), 3–27. https://doi.org/10.1007/s11214-012-9908-y

Min, K., Liu, K., & Li, W. (2014). Signatures of electron Landau resonant interactions with chorus waves from THEMIS observations. *Journal of Geophysical Research: Space Physics*, *119*(7), 5551–5560. https://doi.org/10.1002/2014JA019903

Mozer, F. S., Agapitov, O. V., Blake, J. B., & Vasko, I. Y. (2018). Simultaneous observations of lower band chorus emissions at the equator and microburst precipitating electrons in the ionosphere. *Geophysical Research Letters*, *45*(2), 511–516. https://doi.org/10.1002/2017GL076120

Mozer, F. S., Berthelier, J.-J., Fahleson, U. V., & Fälthammar, C.-G. (1974). *A proposal to measure the quasi-static vector electric field on the low altitude and the elliptic orbiting electrodynamics explorer satellites*. Research Proposal to the National Aeronautics and Space Administration. UCBSSL No. 552/75.

Nagano, I., Yagitani, S., Kojima, H., & Matsumoto, H. (1996). Analysis of wave normal and Poynting vectors of the chorus emissions observed by Geotail. *Journal of Geomagnetism and Geoelectricity*, *48*(3), 299–307. https://doi.org/10.5636/jgg.48.299

Newell, P. (2010). Chorus keeps the diffuse aurora humming. *Nature*, *467*(7318), 927–928. https://doi.org/10.1038/467927a

Ni, B., Thorne, R. M., Meredith, N. P., Horne, R. B., & Shprits, Y. Y. (2011). Resonant scattering of plasma sheet electrons leading to diffuse auroral precipitation: 2. Evaluation for whistler mode chorus waves. *Journal of Geophysical Research*, *116*(A4), A04219. https://doi.org/10.1029/2010ja016233

Nishimura, Y., Bortnik, J., Li, W., Thorne, R. M., Lyons, L. R., Angelopoulos, V., et al. (2010). Identifying the driver of pulsating aurora. *Science*, *330*(6000), 81–84. https://doi.org/10.1126/science.1193186

Omura, Y., Hsieh, Y.-K., Foster, J. C., Erickson, P. J., Kletzing, C. A., & Baker, D. N. (2019). Cyclotron acceleration of relativistic electrons through Landau resonance with obliquely propagating whistler-mode chorus emissions. *Journal of Geophysical Research: Space Physics*, *124*, 2795–2810. https://doi.org/10.1029/2018JA026374

Parrot, M., Santolík, O., Cornilleau-Wehrlin, N., Maksimovic, M., & Harvey, C. C. (2003). Source location of chorus emissions observed by Cluster. *Annals of Geophysics*, *21*(2), 473–480. https://doi.org/10.5194/angeo-21-473-2003

Pedersen, A., Mozer, F., & Gustafsson, G. (1998). Electric field measurements in a tenuous plasma with spherical double probes. In *Measurement techniques in Space plasmas: Fields*. In *Geophysical monograph* (Vol. 103). AGU.

Santolik, O., Chum, J., Parrot, M., Gurnett, D. A., Pickett, J. S., & Cornilleau-Wehrlin, N. (2006). Propagation of whistler mode chorus to low altitudes: Spacecraft observations of structured ELF hiss. *Journal of Geophysical Research*, *111*(A10), A10208. https://doi.org/10.1029/2005JA011462

Santolík, O., & Gurnett, D. A. (2002). Propagation of auroral hiss at high altitudes. *Geophysical Research Letters*, *29*(10), 119-1–119-4. https://doi.org/10.1029/2001GL013666

Santolik, O., Gurnett, D. A., Pickett, J. S., Chum, J., & Cornilleau-Wehrlin, N. (2009). Oblique propagation of whistler mode waves in the chorus source region. *Journal of Geophysical Research*, *114*(A12), A00F03. https://doi.org/10.1029/2009JA014586

Santolik, O., Gurnett, D. A., Pickett, J. S., Parrot, M., & Cornilleau-Wehrlin, N. (2004). A microscopic and nanoscopic view of storm-time chorus on 31 March 2001. *Geophysical Research Letters*, *31*(2), L02801. https://doi.org/10.1029/2003GL018757

Santolik, O., Gurnett, D. A., Pickett, J. S., Parrot, M., & Cornilleau-Wehrlin, N. (2005). Central position of the source region of storm-time chorus, Planet. *Space Science*, *53*(1–3), 299–305. https://doi.org/10.1016/j.pss.2004.09.056

Santolík, O., Parrot, M., & Lefeuvre, F. (2003). Singular value decomposition methods for wave propagation analysis. *Radio Science*, *38*(1), 1010. https://doi.org/10.1029/2000RS002523

Santolík, O., Pickett, J. S., Gurnett, D. A., & Storey, L. R. O. (2002). Magnetic component of narrowband ion cyclotron waves in the auroral zone. *Journal of Geophysical Research*, *107*(A12), SMP17-1–SMP17-14. https://doi.org/10.1029/2001JA000146

Shumko, M., Blum, L. W., & Crew, A. B. (2021). Duration of individual relativistic electron microbursts: A probe into their scattering mechanism. *Geophysical Research Letters*, *48*(17), e2021GL093879. https://doi.org/10.1029/2021GL093879

Shumko, M., Turner, D. L., O'Brien, T. P., Claudepierre, S. G., Sample, J., Hartley, D. P., et al. (2018). Evidence of microbursts observed near the equatorial plane in the outer van Allen radiation belt. *Geophysical Research Letters*, *45*(16), 8044–8053. https://doi.org/10.1029/2018GL078451

Summers, D., Omura, Y., Nakamura, S., & Kletzing, C. A. (2014). Fine structure of plasmaspheric hiss. *Journal of Geophysical Research: Space Physics*, *119*(11), 9134–9149. https://doi.org/10.1002/2014JA020437

Taubenschuss, U., Santolik, O., Breuillard, H., Li, W., & Contel, O. L. (2016). Poynting vector and wave vector directions of equatorial chorus. *Journal of Geophysical Research: Space Physics*, *121*(12), 11912–11928. https://doi.org/10.1002/2016JA023389

Teng, S., Tao, X., Li, W., Qi, Y., Gao, X., Dai, L., et al. (2018). A statistical study of the spatial distribution and source-region size of chorus waves using Van Allen Probes data. *Annals of Geophysics*, *36*(3), 867–878. https://doi.org/10.5194/angeo-36-867-2018

Thorne, R., Ni, B., Tao, X., & Meredith, N. P. (2010). Scattering by chorus waves as the dominant cause of diffuse auroral precipitation. *Nature*, *467*(7318), 943–946. https://doi.org/10.1038/nature09467

Thorne, R. M., Li, W., Ni, B., Ma, Q., Bortnik, J., Chen, L., et al. (2013). Rapid local acceleration of relativistic radiation belt electrons by magnetospheric chorus. *Nature*, *504*(7480), 411–414. https://doi.org/10.1038/nature12889

Tsurutani, B. T., Falkowski, B. J., Pickett, J. S., Santolik, O., & Lakhina, G. S. (2015). Plasmaspheric hiss properties: Observations from polar. *Journal of Geophysical Research: Space Physics*, *120*(1), 414–431. https://doi.org/10.1002/2014JA020518

Tsurutani, B. T., & Smith, E. J. (1974). Postmidnight chorus: A substorm phenomenon. *Journal of Geophysical Research*, *79*(1), 118–127. https://doi.org/10.1029/JA079i001p00118

Tyler, E., Breneman, A., Cattell, C., Wygant, J., Thaller, S., & Malaspina, D. (2019). Statistical occurrence and distribution of high-amplitude whistler mode waves in the outer radiation belt. *Geophysical Research Letters*, *46*(5), 2328–2336. https://doi.org/10.1029/2019GL082292

Wang, D., Shprits, Y. Y., Zhelavskaya, I. S., Agapitov, O. V., Drozdov, A. Y., & Aseev, N. A. (2019). Analytical chorus wave model derived from Van Allen Probe observations. *Journal of Geophysical Research: Space Physics*, *124*(2), 1063–1084. https://doi.org/10.1029/2018JA026183

Wygant, J. R., Bonnell, J. W., Goetz, K., Ergun, R. E., Mozer, F. S., Bale, S. D., et al. (2013). The electric field and waves instruments on the radiation belt storm probes mission. *Space Science Reviews*, *179*(1–4), 183–220. https://doi.org/10.1007/s11214-013-0013-7

Zhu, H., Su, Z., Xiao, F., Zheng, H., Wang, Y., Shen, C., et al. (2015). Plasmatrough exohiss waves observed by Van Allen Probes: Evidence for leakage from plasmasphere and resonant scattering of radiation belt electrons. *Geophysical Research Letters*, *42*(4), 1012–1019. https://doi.org/10.1002/2014GL062964